UNIVERSITY OF
BATH

University of Bath

Hierarchical Growth of TiO₂ Nanosheets on Anodic ZnO Nanowires for High Efficiency Dye-Sensitized Solar Cells

David O. Miles[a,+], Chang Soo Lee[b,+], Petra J. Cameron[c], Davide Mattia[d,*], Jong Hak Kim[b,*]

[a]*Centre for Sustainable Chemical Technologies, University of Bath, Bath, BA2 7AY UK.*

[b]*Department of Chemical and Biomolecular engineering, Yonsei University, Seoul, 120-749, South Korea*

[c]*Department of Chemistry, University of Bath, Bath BA2 7AY, UK*

[d] *Department of Chemical Engineering, University of Bath, Bath, BA2 7AY, UK*

[*] To whom correspondence should be addressed

Dr. Davide Mattia

E-mail: D.Mattia@bath.ac.uk

Prof. Jong Hak Kim

Tel: +82-2-2123-5757; Fax: +82-2-312-6401

E-mail: jonghak@yonsei.ac.kr

[+] These authors contributed equally to this publication.

Abstract

We present a novel route to hierarchical core-shell structures consisting of an anodic ZnO nanowire core surrounded by a shell of TiO_2 nanosheets (ZNW@TNS). This material combines the beneficial properties of enhanced electron transport, provided by the nanowire core, with the high surface area and chemical stability of the TiO_2 shell. Quasi-solid-state dye-sensitized solar cells (qssDSSCs) are prepared using different quantities of either the bare ZnO nanowires or the hierarchical nanowire structures and the effect on cell performance is examined. It is found that whilst the addition of the bare ZnO nanowires results in a decrease in cell performance, significant improvements can be achieved with the addition of small quantities of the hierarchical structures. Power conversion efficiencies of up to 7.5 % are achieved under 1 Sun, AM 1.5 simulated sunlight, with a ~30 % increase compared to non-hierarchical mesoporous TiO_2 films. A solid-state DSSC (ssDSSC) with a single component solid polymer also exhibits excellent efficiency of 7.2%. The improvement in cell performance is related to the improved light scattering, surface area and electron transport properties *via* the use of reflectance spectroscopy, BET surface area measurements and electrochemical impedance spectroscopy.

Keywords: ZnO nanowire; TiO_2 nanosheet; core-shell; dye-sensitized solar cells; solid-state electrolyte; graft copolymer.

1. Introduction

Dye-sensitized solar cells (DSSCs) are an attractive photovoltaic technology for application in a wide range of markets due to their low cost, aesthetic appeal and compatibility with flexible substrates [1]. Since their first report in 1991 by Grätzel et al. they have attracted significant interest from the research community, leading to power conversion efficiencies of over 14 % [2-4]. Key to the success of DSSCs is the mesoporous TiO_2 scaffold that provides a high surface area for dye-adsorption and allows conduction of photo-generated electrons to the collecting electrode. Many different attempts have been made to improve the performance of DSSCs by modifying, or finding alternatives to, the mesoporous TiO_2 layer. These include the introduction of light scattering layers to improve light absorption [5], the use of templating polymers to form ordered porous networks [6,7] and the introduction of a wide range of different nanostructures to improve charge transport or increase surface areas [8].

The use of one-dimensional nanostructures, such as nanowires, has commonly been proposed as a route to enhanced electron transport within DSSCs, particularly when high electron mobility materials such as ZnO are used [9-12]. However, improvements in charge transport have often been accompanied by significant losses in light absorption due to the low surface areas of crystalline nanowires compared to nanoparticles [13,14]. To enhance the surface areas of one-dimensional nanostructures, hierarchical structures have been investigated, which typically involve the growth of high surface area nanostructures onto the nanowire surface. Such approaches have shown promise in enhancing cell performances compared to the use of bare nanowires structures [15-20].

Another successful route has been to combine two different materials, forming core-shell nanostructures [21]. Here the one-dimensional nanomaterial at the core is a high electron mobility material, such as ZnO or SnO_2, and the shell is TiO_2, which provides the best compatibility with

commonly used dyes and electrolytes [22-25]. Recently, TiO_2-ZnO nanowire or nanosheet composites have also been reported as efficient photoanodes for DSSCs [26-30]. We have previously demonstrated that the use of hierarchical nanostructures consisting of a TiO_2 nanosheet shell surrounding a SnO_2 nanotube core can provide significant enhancements in cell performance when employed in solid state DSSCs (ssDSSCs) [31]. By using the hierarchical nanostructures as additives within an organised mesoporous TiO_2 film, power conversion efficiencies of up to 7.7 % were achieved, some of the highest reported for ssDSSCs.

Herein, we report the formation of novel hierarchical nanostructures consisting of a polycrystalline ZnO nanowire core surrounded by a shell of TiO_2 nanosheets and their application within quasi solid-state DSSCs (qssDSSCs). The polycrystalline ZnO core is produced via the rapid electrochemical anodization of zinc foil and can be modified with TiO_2 nanosheets through a simple solvothermal growth method [31,32]. It should be noted that the electrochemical anodization synthesis of the ZNW core comprised of a much simpler process, with shorter reaction times compared to those of the SnO_2 nanotubes used in our previous work, or solvothermal methods using autoclaves. Through addition of small quantities of the hierarchical nanowire structures to an organised mesoporous TiO_2 film power conversion efficiencies were increased from 5.8 % to 7.5 % which are among some of the highest reported efficiencies for qssDSSCs. The improvements in cell performance are attributed to the enhanced light scattering, improved electron transport and increased surface areas of the hierarchical nanowires.

2. Experimental Section

2.1. Materials

Poly(vinyl chloride) (PVC, $M_n \sim 55,000$ g/mol), poly(oxyethylene methacrylate) (POEM, $M_n \sim 500$ g/mol), 1,1,4,7,10,10-hexamethyltriethylenetetramine (HMTETA, 97 %), copper (I) chloride (CuCl,

> 99 %), hydrochloric acid (HCl, 37 %), titanium diisopropoxide bis(acetylacetonate) (75 wt.% in isopropanol), chloroplatinic acid hexahydrate ($H_2PtCl_6 \cdot 6H_2O$, ≥ 37.50 % Pt basis), 1-methyl-3-propylimidazolium iodide (MPII), poly(ethylene glycol) (PEG, M_n ~ 10,000 g/mol), iodine (I_2, ≥99 %), lithium iodide (LiI, 99.9 %), diethylenetriamine (DETA), titanium (IV) chloride ($TiCl_4$, 99.9 %), benzyl alcohol (anhydrous, 99.8 %), sodium bicarbonate ($NaHCO_3$, ACS reagent > 99.7 %) and acetone (> 99.5 %) were all purchased from Sigma-Aldrich and were used as received without further purification. Zinc foil (99.98 %, 0.25 mm thickness) was purchased from Alfa-Aesar, and Fluorine-doped tin oxide (FTO) conductive glass (TEC8, 8 ohms sq.-1, 2.3 mm thick) was purchased from Pilkington, France, and washed before using, with ethanol, acetone, and ethanol under sonication for 30 min in sequence, respectively.

2.2 Synthesis of ZnO Nanowires

ZnO nanowires (ZNW) were produced by the electrochemical anodization of zinc foil, full details of which have been previously published [32,33]. Prior to anodization, zinc foils were annealed at 300 °C for 1 hour in air followed by degreasing with acetone in an ultrasonic bath for 10 minutes. The clean zinc foil was applied as the anode in a two-electrode cell with a stainless steel plate held parallel to the anode at a distance of 10 mm acting as the cathode. The active area of the zinc anode was controlled using kapton tape, exposing a 13.5 cm^2 area on one side of the zinc foil. The anodization was conducted in an aqueous electrolyte of $NaHCO_3$ (0.05 M) with constant stirring. The temperature of the electrolyte was controlled at 20 °C using a jacketed beaker linked to a refrigerated circulating bath. Anodizations were undertaken for 15 minutes at a constant voltage of 5 V provided by a DC power supply (Agilent, E3634A) to give rise to uniform nanowire films with a typical film thickness of 50 μm. After anodization, the anodic films were washed thoroughly with deionised water to remove any excess electrolyte from the surface. The foils were then dried under a gentle

flow of argon gas and annealed at 300 °C for 1 h in air using a ramping rate of 1°C min^{-1}. Finally, the nanowire films were scraped from the substrates to form a powder.

2.3 Synthesis of ZnO nanowire@TiO$_2$ nanosheets

ZnO nanowires coated with TiO$_2$ nanosheets (ZNW@TNS) were synthesized by a hydrothermal reaction using TTIP and DETA as the precursor and structure directing agent of TiO$_2$ nanosheets, respectively [31]. 0.1 g of ZNW was dispersed in 40 ml of isopropyl alcohol (IPA) under sonication for 30 min. Next, 0.3 ml of TTIP and DETA were added into the ZNW dispersion and further stirred for 30 min to prepare a homogeneous solution. It was transferred to a Teflon-lined autoclave and kept at 200 °C in an oven for 24 h. After cooling down to room temperature, the white product was collected *via* centrifugation at 9,000 rpm or *via* natural precipitation for 24 h. It was further washed with ethanol several times, dried at 80 °C in a vacuum oven for 24 h and annealed at 450 °C for 30 min to remove the organic residue. For the fabrication of photoanodes, the ZNW@TNS collected by natural precipitation method was used.

2.4 Device Fabrication

First, a compact blocking layer was deposited on the FTO glass by spin-coating a 0.1 M titanium diisopropoxide bis(acetylacetonate) solution in n-butanol and annealing at 450 °C for 30 min. The organized mesoporous (OM) TiO$_2$ was constructed on the blocking layer with an amphiphilic graft copolymer, PVC-*g*-POEM, as the sacrificing template, according to our previously reported literature [34] 4, 8 and 12 wt. % of ZNW or ZNW@TNS powder was dispersed in 2 ml of THF under ultrasonication and 0.2 g of PVC-*g*-POEM copolymer was sequentially dissolved in the above solution overnight. Separately, hydrophilic TiO$_2$ nanoparticles (pre-TiO$_2$) were prepared by adding 1.5 ml of TiCl$_4$ and 50 ml of benzyl alcohol in 10 ml of toluene and heating at 70 °C for 15 h. The

6

pre-TiO$_2$ powder was collected *via* centrifugation at 12,000 rpm for 30 min. 0.35 g of as-prepared pre-TiO$_2$ and 0.1 ml of HCl (for OM-TiO$_2$ w/ HCl photoanode) or H$_2$O (for OM-TiO$_2$ w/ H$_2$O photoanode) was dissolved in the PVC-*g*-POEM/ZNW or ZNW@TNS solution overnight to form the highly viscous paste of polymer/inorganic hybrid solution. It was directly coated onto the blocking layer on FTO glass using a doctor-blade technique. The films were annealed at 450 °C for 30 min to form the ZNW or ZNW@TNS embedded OM structure. For the preparation of Pt counter electrodes, 0.01 M of a H$_2$PtCl$_6\cdot$6H$_2$O solution in 2-propanol was spin-coated on the FTO glass and annealed at 450 °C for 30 min.

The photoanodes were immersed in 10^{-4} M Ru(dcbpy)$_2$(NCS)$_2$ dye (dcbpy = 2,2-bipyridyl-4,4-dicarboxylato) N719 dye solution in absolute ethanol at room temperature for 24 h to sensitize the dye molecules on the surface of the photoanodes. The dye-sensitized photoanodes were washed with ethanol to remove the physically adsorbed dye molecules. The quasi-solid-state, nanogel electrolyte was prepared by dissolving PEG, MPII, LiI, and I$_2$ in acetonitrile, according to our previously reported literature [35]. In the case of the solid-state electrolyte, poly((1-(4-ethenylphenyl)methyl)-3-butyl-imidazolium iodide) (PEBII) was synthesized and employed using a previously reported synthesis method [36]. Briefly, the as-prepared electrolyte was cast onto the photoanode by drop-casting low and high concentration electrolytes several times to form well-penetrated electrolyte/TiO$_2$ photoanodes. The conductive sides of both the photoanode and counter electrode were pressed together and the electrolyte was slowly allowed to evaporate. The electrodes were attached with epoxy resin and dried in a vacuum oven at room temperature overnight to fabricate the DSSC devices.

2.5 Characterisation

The structure of ZNW, ZNW@TNS, and photoanodes were characterized using a field-emission

scanning electron microscope (FE-SEM, SUPRA 55VP, Carl Zeiss, Germany) and energy-filtering transmission electron microscope (EF-TEM, Philips CM30) operated at 120 kV. X-ray photoelectron spectroscopy (XPS, K-alpha, Thermo VG, U.K.) was operated with a X-ray source of monochromated Al Kα and with a sampling depth less than 10 nm range. A specific surface area of OM, ZNW and ZNW@TNS film series were confirmed by using N_2 adsorption/desorption data (BELCAT II, BEL Japan Inc., Japan) with Brunauer-Emmett-Teller (BET) analysis. The UV-visible light spectra were measured in the wavelength region from 300 to 800 nm with a UV-visible spectrophotometer (Hewlett-Packard, Hayward, CF). The dye loading was measured by dipping the dye-sensitized photoanodes with an active area of 0.64 cm^2 into the 0.1 M NaOH ethanolic solution with 1:1 volume ratio of ethanol and deionized water. It was further stirred for 1 h to obtain a homogeneous solution. UV-visible light absorption spectroscopy was employed to calculate the dye loading using the peak value at 515 nm, according to the Beer-Lambert law: $A = \varepsilon l c$ where A is the absorbance at 515 nm, ε ($= 14,100$/M cm) is the molar extinction coefficient of N719 dye at 515 nm, l is the light path length in the cell, and c is the N719 dye concentration.

The electrochemical performances of DSSCs were evaluated by measuring the short-circuit current (J_{sc}, mA/cm^2), open-circuit voltage (V_{oc}, V), fill factor (FF), and energy conversion efficiency (η, %). Those photovoltaic parameters were calculated by employing J-V measurements with a Keithley Model 2400 and a 1,000 W xenon lamp (Oriel, 91193). The light source was homogeneous over an 8 in. x 8 in. area and was calibrated with a silicon solar cell (Fraunhofer Institute for Solar Energy System, Mono-Si + KG filter, Certificate No. C-ISE269) with one sunlight intensity (100 mW/cm^2), verified by a NREL-calibrated Si solar cell (PV measurements Inc.). The incident photon-to-current conversion efficiency (IPCE) spectra were measured as a function of wavelength from 300 to 800 nm (McScience, K3100). The selected area electron diffraction (SAED) pattern was measured using a high-resolution transmission electron microscope (HR-TEM, JEM-

3010, JEOL). Electrochemical impedance spectroscopy (EIS) was conducted on the cells at 1 sun, provided by a Xenon arc lamp (USHIO Inc., Japan), and open circuit voltage within the frequency range of 0.05 Hz to 0.1 MHz (CompactStat, Ivium Technologies, The Netherlands).

3. Result and discussion

3.1 Synthesis of ZNW and ZNW@TNS

The ZnO nanowires (ZNW) were synthesized using an electrochemical anodization technique followed by annealing in air, full details of which can be found in a previous publication [32]. After synthesis, the nanowires were removed from the zinc substrate they were grown on and sonicated to fragment the nanowires into sections with lengths typically between 1 and 10 μm. It can be clearly observed in the SEM and TEM micrographs of the ZNW structures (Fig. 1a,d) that the nanowires have a characteristic slit-type pore structure along their length, which arises during the annealing treatment. TEM analysis revealed that the nanowires had an average diameter of 160 ± 60 nm and were composed of multiple small ZnO nanoparticles with an average diameter of ~9 nm.

The ZnO nanowire@TiO$_2$ nanosheets (ZNW@TNS) particles were collected *via* different separation methods, which were centrifugation and natural precipitation. From Fig. 1b,c, the TiO$_2$ nanosheets were well coated on the surface of ZNW without any vacancies. However, there were considerable by-products in the ZNW@TNS nanoparticles collected with centrifugation, such as aggregated particles of TiO$_2$ nanosheets, as shown in Fig. 1b. It was also confirmed from the TEM micrograph in Fig. 1e that excess nanosheets were present after the centrifugation process, which separated all of the heavier particles from the solvent. In order to separate the pure ZNW@TNS from the TiO$_2$ nanosheet aggregates, a natural precipitation method was employed to settle the heavier ZNW@TNS whilst keeping the TiO$_2$ nanosheet aggregates in solution. When the upper cloudy solution was removed and the bottom white precipitate was washed with ethanol several times, the

pure ZNW@TNS particles were obtained as shown in Fig. 1c. Fig. 1f represents the EF-TEM image of ZNW@TNS obtained by natural precipitation showing that the TiO_2 nanosheet aggregate by-products were totally removed from the ZNW@TNS. Therefore, the ZNW@TNS particles from the natural precipitation method were used as the additives in OM-TiO_2 photoanodes.

The ZNW and ZNW@TNS structures were further characterized using HR-TEM and SAED, as shown in Fig. S1. From the HR-TEM micrographs of ZNW (Fig. S1a, b), clear lattice planes of ZnO were observed with d-spacing values of 0.284 nm. According to the previously reported literature [12], it was assigned to the (002) facet of ZnO. In the case of ZNW@TNS (Figure S1c,d), there were two major crystal lattices observed with d-spacing values of 0.266 nm and 0.362 nm, which represents the ZnO and (101) facet of TiO_2 respectively.

X-ray photoelectron spectroscopy (XPS) was also employed to analyse the ZNW and ZNW@TNS structures by comparing the elements on the surface of each particle within the specific regions associated with Zn, Ti, O and N (Fig. 2). From Fig. 2a, the Zn 2p components appeared as two split peaks at 1045 eV and 1022 eV for both ZNW and ZNW@TNS, due to the spin-orbital splitting behaviour of Zn $2p_{1/2}$ and Zn $2p_{3/2}$ orbitals, respectively. The Zn 2p peak positions were in good agreement with the previously reported peak positions of 2D ZnO nanowires or nanorods [37-39]. Similarly, as shown in Fig. 2b, the split peaks of Ti 2p appeared at 465 eV for Ti $2p_{1/2}$ and 459 eV for Ti $2p_{3/2}$ orbitals from Ti^{4+} in the anatase phase of crystalline TiO_2 [40]. These peaks were only observed for ZNW@TNS due to the anatase phase of TNS coated on the surface of ZNW. From Fig. 2c, two peaks were observed at 530.4 and 531.6 eV after fitting a Gaussian curve. According to the previously reported literature [41-44], the O 1s peaks at 530.4 and 531.6 eV were assigned to the O 1s core-level of bulk ZnO and to surface hydroxyl groups with chemical or physical adsorption. The difference of O 1s binding energy value between the peaks was attributed to the lower electronegativity of zinc (1.7) than hydrogen (2.1), which results in a smaller binding energy for the

10

bulk Zn-O group than for the O-H functional group. For ZNW@TNS, the relative O 1s peak of O-H group exhibited a lower intensity compared to that of ZNW due to the growth of anatase TNS on the surface of ZNW. Moreover, in the N 1s XPS region, two overlapping peaks were observed at 400.7 and 399.2 eV after fitting for the ZNW@TNS, which was attributed to the chemisorbed NO_x or NH_3 and O-Ti-N groups respectively. This phenomenon was mainly attributed to the higher electronegativity of oxygen (3.5) than titanium (1.5), resulting in a decrease of electron density of nitrogen and, therefore, an increase in binding energy [40]. These results indicate that N-doped TNS was synthesized on the surface of ZNW which arises due to the N content in DETA during the hydrothermal growth.

3.2 Photoanode Preparation

In previous reports, HCl has typically been used to induce microphase separation of the PVC-g-POEM graft copolymer template and to better disperse the pre-TiO_2 nanoparticles [45,46]. However, as ZnO is readily dissolved in acidic conditions, it was necessary to replace the HCl with H_2O to form the OM-TiO_2 films. It can be observed from Fig. 3a, b that OM-TiO_2 synthesized with pure H_2O exhibited a mesoporous structure. However, compared with the OM-TiO_2 films produced with HCl in the PVC-*g*-POEM/pre-TiO_2 hybrid solution, a large number of cracks were present due to the poor dispersion of pre-TiO_2 (Fig. 3c, d).

As the ZNW particles were added in the PVC-*g*-POEM/pre-TiO_2 hybrid solution, the OM film structure appeared to improve, without any significant cracking until the addition of 8 wt. % of ZNW particles (Fig. 4a-d). 4, 8, and 12 wt. % of ZNW were added in the solution and the resulting photoanodes were designated as ZNW1, ZNW2 and ZNW3, respectively. We expect that the hydrophilic POEM domain was well organized along with the hydrophilic –OH functional groups at the surface of ZNW (Fig. 2c). This could explain how the ZNW plays a pivotal role in fabricating the

11

OM structure without any cracks. This well-connected structure is highly important in transporting the electrons through the conduction band of the TiO_2. Moreover, the dye loading ability of the films would likely be increased as the number of large cracks or vacancies were reduced for ZNW1 and ZNW2. However, when 12 wt. % of ZNW was added in OM-TiO_2 cracks began to appear, which were attributed to the deformation of the polymer.

To fabricate the ZNW@TNS embedded OM-TiO_2 photoanodes 4, 8 and 12 wt. % of ZNW@TNS were again added in the solution, with the resultant photoanodes named as ZNW@TNS1, ZNW@TNS2 and ZNW@TNS3, respectively. In good agreement with the morphology of OM-TiO_2 synthesized by the addition of ZNW, the OM structure was also observed to be crack free for these photoanodes up to ~~12~~ 8 wt.% (Fig. 5). This demonstrates that the appropriate addition of ZNW@TNS core—shell particle was important for synthesizing OM-TiO_2 without the use of HCl. From the cross-sectional FE-SEM micrographs in Fig. S2, the thickness of photoanodes was 5.5 ± 0.2 μm, except for the OM-TiO_2 photoanode synthesized with pure deionized H_2O. This was attributed to the poor dispersion of preformed TiO_2 without HCl.

To evaluate the optical properties of the photoanodes, UV-visible (UV-vis) reflectance spectroscopy was employed to measure the light scattering ability of photoanodes (Fig. 6). The transparent OM photoanode with HCl exhibited a low light reflectance of around 15 % of the maximum value, resulting from the well-organized mesoporous structure without any significant cracks. However, the reflectance of the OM photoanode with H_2O was the highest among all of the samples due to the severe cracks and less organised structure with aggregated TiO_2 particles. Therefore, the OM with HCl was selected as a reference sample to make a precise comparison of ZNW and ZNW@TNS photoanodes. Generally, the ZNW and ZNW@TNS photoanodes exhibited higher light scattering abilities than OM with HCl. This was attributed to the addition of nanostructured ZNW or ZNW@TNS particles, resulting in a significant difference of refractive

12

index with air/OM-TiO$_2$ surroundings [47]. Moreover, the higher light reflectance of the ZNW or ZNW@TNS photoanodes was observed to increase as the proportion of ZNW or ZNW@TNS nanoparticles was increased. The above result implies that the addition of ZNW or ZNW@TNS was an important factor in increasing the light scattering ability of the photoanodes, which in turn has the potential to enhance the absorption of light. These trends in the UV-visible reflectance spectra could also be observed by eye in the relative opacity of the films (Fig. 6b).

3.3 Device Performance

Photovoltaic parameters of the quasi-solid-state dye-sensitized solar cells (qssDSSCs) with nanogel electrolyte were calculated by analysing current density-voltage (*J-V*) curves (Fig. 7a) and are summarized in Table 1. The conversion efficiency of qssDSSCs using ZNW photoanodes was always lower than that of OM. The lower efficiency of the ZNW series than OM results from the lower J_{sc}, attributed to the poor dye loading and recombination of photoexcited electrons between ZNW/electrolyte from direct exposure of ZNW, despite the greater light scattering ability than OM (Fig. S3) [48]. However, the open-circuit voltage (V_{oc}) was found to be enhanced when more ZNW nanoparticles were added, compared with bare OM. This enhancement of V_{oc} was attributed to the faster electron mobility in bulk phases of ZnO than TiO$_2$ and to the slightly higher conduction band edge of ZnO compared to TiO$_2$ [49,50].

To overcome the drawbacks of ZNW, or the poor dye loading ~~due to the low specific surface area~~, ZNW@TNS core-shell nanoparticles were added to the OM photoanode. In addition to the relative increase in specific surface area caused by the use of ZNW@TNS rather than ZNW, it is thought that the improved adhesion of ZNW@TNS within the OM-TiO$_2$ matrix would also provide an improved dye loading, due to a reduction in film cracking. In the case of ZNW, severe cracks or defects were present in the photoanode films and in turn, caused a significant decrease in dye loading

13

compared with their actual specific surface area. This is believed to be related to the large void areas within the cracks that are not capable of adsorbing dye. The J_{sc} of ZNW@TNS1 (17.36 mA cm^{-2}) was the highest among all of the photoanodes, which can be attributed to the enhanced dye loading and slightly higher specific surface area. The addition of small quantities of ZNW@TNS core-shell structures achieved the enhancement of J_{sc} in four ways: 1) the increased specific surface area due to the TNS which results in higher dye loadings (Table 1), 2) the faster electron mobility of one-dimensional ZnO than TiO$_2$ in bulk phases, 3) the suppression of recombination between ZNW/electrolyte, and 4) the enhanced light scattering effect. Particularly, the recombination rate can be reduced due to the formation of a radial surface field within the core-shell structure [23]. It should also be noted that the V_{oc} of ZNW@TNS1 was slightly increased from 0.69 to 0.72 V compared to OM. This resulted in a conversion efficiency of 7.46 % for ZNW@TNS1, which is 29 % higher than that of OM (5.78 %). Therefore, the incorporation of ZNW@TNS core-shell nanostructures in OM-TiO$_2$ played a pivotal role to enhance both J_{sc} and V_{oc} by providing a high surface area barrier layer around the ZNW. However, further addition of ZNW@TNS particles in OM-TiO$_2$ resulted in lower conversion efficiency. This is likely due to an excessive amount of ZNW@TNS resulting in a less-organized OM-TiO$_2$ structure and causing cracks in the photoanode. (Fig. 5f)

To further investigate the photocurrent density of the OM, ZNW and ZNW@TNS photoanodes, the incident photon-to-current conversion efficiency (IPCE) was measured (Fig. 7b) as a function of wavelength (λ) according to the following relationship:

$$IPCE\ (\%) = \frac{1240 \wedge Jsc}{\lambda \times p_{in}} \times 100$$

where p_{in} is the incident solar power. Among the samples, the ZNW@TNS1 exhibited the highest IPCE value from 300 to 800 nm, in good agreement with the J_{sc} value from the J-V curve. In particular, the IPCE value in the wavelengths from 450 to 550 nm was largely increased due to the

14

following two factors: 1) the enhanced light scattering effect of ZNW@TNS1 in that region compared with bare OM, and 2) the higher dye loading of ZNW@TNS1 (125.5 nmol cm^{-2}) than that of OM (110.2 nmol cm^{-2}). As a UV-visible light absorption peak of N719 dye was observed from 500 to 550 nm, a significant improvement of current density in that region was obtained. The IPCE of the other samples was generally decreased due to the low dye loading, severe cracks in the case of ZNW3 and ZNW@TNS3, and an aggregated, less-organized morphology of the photoanodes. (Fig. 5c, 5f) The appropriate incorporation of ZNW@TNS core-shell nanoparticles is, therefore, important, as although photocurrent densities were significantly enhanced for small quantities (4 wt.%) further increases in ZNW@TNS quantities resulted in the opposite effect.

The cells were also analysed by electrochemical impedance spectroscopy (EIS) under 1 sun illumination and open circuit voltage to determine resistances associated with the various electron transfer processes occurring within the cells. The Nyquist plots of both the ZNW and ZNW@TNS cell series are shown in Fig. S4 along with a full description of the equivalent circuit analysis. The values obtained for the charge transfer resistance at the semiconductor/electrolyte interface were found to generally increase upon the addition of both ZNW and ZNW@TNS structures to the OM film. The increase was found to be significant in the case of ZNW2, ZNW3 and ZNW@TNS3, however, only slight deviations in charge transfer resistance were found for the remaining photoanodes compared to OM. The highest performing cells (ZNW@TNS1) were found to have a slightly higher charge transfer resistance than their ZNW equivalent. This slight difference might be a result of the core-shell structure of these nanowires, however, given that this difference is only small it might be the case that the majority of the efficiency increase for ZNW@TNS is a result of the increased dye loading rather than reduced recombination.

The ZNW@TNS1 photoanode, which exhibited the highest efficiency among the qssDSSCs

using other photoanodes, was further employed to confirm the performance in ssDSSCs. A single component solid-state polymer, i.e. PEBII, was employed to fabricate ssDSSCs, according to our previously reported method [36]. The conversion efficiency of ssDSSCs using a PEBII electrolyte and ZNW@TNS1 photoanode achieved 7.2% under one sun illumination (Fig. 7c), which is a much higher value than neat OM or commercially available photoanodes reported previously in the literature [31]. This efficiency is among the highest values reported for N719-based ssDSSCs [34-36,50-56] The high efficiency of ZNW@TNS1 was attributed to the π-π stacking behaviour and low glass transition temperature of the PEBII electrolyte. Therefore, the multi-functional, core-shell ZNW@TNS nanoparticles play a pivotal role to enhance the efficiency by the improvement of OM-TiO_2 morphology, enhancement of light reflectance, faster electron transport than neat OM, and suppressed electron recombination between ZNW and electrolyte.

4. Conclusions

In this report, we demonstrate the production of novel core-shell hierarchical ZNW@TNS structures through solvothermal growth on anodic ZnO nanowires, as confirmed by FE-SEM, HR-TEM and XPS. These nanostructures proved advantageous when incorporated into well-organized mesoporous (OM) TiO_2 photoanodes using a PVC-*g*-POEM graft copolymer template and hydrophilically preformed TiO_2. In particular, the introduction of ZNW@TNS compensated the drawback of bare ZNW by suppressing the recombination at the ZNW/electrolyte interface and by enhancing dye loading due to the large surface areas of TNS. Furthermore, the ZNW@TNS proved highly advantageous due to the enhanced electron transport and light scattering of the one-dimensional nanostructures. The addition of small quantities of ZNW@TNS within the qss-DSSCs resulted in a high conversion efficiency of 7.46%, which is 29 % higher than with bare OM (5.78%). The

16

efficiency of ssDSSCs fabricated using a single component PEBII solid polymer also reached a high value of 7.2%, which is among the highest values reported for N719-based ssDSSCs. We therefore propose that the use of core-shell hierarchical structures as additives within photoanodes is an effective route to enhancing the power conversion efficiency of dye-sensitized solar cells.

5. Acknowledgements

References

1. M. Graetzel, Acc. Chem. Res. 42 (2009) 1788-1798.

2. S. Mathew, A. Yella, P. Gao, R. Humphry-Baker, B. F. E. Curchod, N. Ashari-Astani, I. Tavernelli, U. Rothlisberger, M. K. Nazeeruddin and M. Graetzel, Nat. Chem. 6 (2014) 242-247.

3. B. Oregan and M. Graetzel, Nature 353 (1991) 737-740.

4. K. Kakiage, Y. Aoyama, T. Yano, K. Oya, J. Fujisawa and M. Hanaya, Chemical Communications 51 (2015) 15894-15897.

5. Z. S. Wang, H. Kawauchi, T. Kashima and H. Arakawa, Coord. Chem. Rev. 248 (2004) 1381-1389.

6. M. Zukalova, A. Zukal, L. Kavan, M. K. Nazeeruddin, P. Liska and M. Gratzel, Nano Lett. 5 (2005) 1789-1792.

7. Y. Xiong, D. He, Y. Jin, P. J. Cameron and K. J. Edler, J. Phys. Chem. C 119 (2015) 22552-22559.

8. Q. Zhang and G. Cao, Nano Today 6 (2011) 91-109.

9. I. Gonzalez-Valls and M. Lira-Cantu, Energy Environ. Sci. 2 (2009) 19-34.

10. M. Yu, Y. Z. Long, B. Sun and Z. Y. Fan, Nanoscale 4 (2012) 2783-2796.

11. B. Weintraub, Z. Zhou, Y. Li and Y. Deng, Nanoscale 2 (2010) 1573-1587.

12. M.-L. Zhang, F. Jin, M.-L. Zheng, J. Liu, Z.-S. Zhao and X.-M. Duan, RSC Adv. 4 (2014) 10462-10466.

13. M. Law, L. E. Greene, J. C. Johnson, R. Saykally and P. D. Yang, Nat. Mater. 4 (2005) 455-459.

14. J. B. Baxter and E. S. Aydil, Appl. Phys. Lett. 86 (2005) 053114.

15. H.-M. Cheng, W.-H. Chiu, C.-H. Lee, S.-Y. Tsai and W.-F. Hsieh, J. Phys. Chem. C 112 (2008) 16359-16364.

16. V.-M. Guerin and T. Pauporte, Energy Environ. Sci. 4 (2011) 2971-2979.

17. J. Qiu, M. Guo, Y. Feng and X. Wang, Electrochim. Acta 56 (2011) 5776-5782.

18. H. Dai, Y. Zhou, Q. Liu, Z. Li, C. Bao, T. Yu and Z. Zhou, Nanoscale 4 (2012) 5454-5460.

19. L.-Y. Chen and Y.-T. Yin, Nanoscale 5 (2013) 1777-1780.

20. R. Gao, J. Tian, Z. Liang, Q. Zhang, L. Wang and G. Cao, Nanoscale 5 (2013) 1894-1901.

21. N. O. V. Plank, I. Howard, A. Rao, M. W. B. Wilson, C. Ducati, R. S. Mane, J. S. Bendall, R. R. M. Louca, N. C. Greenham, H. Miura, R. H. Friend, H. J. Snaith and M. E. Welland, J. Phys. Chem. C 113 (2009) 18515-18522.

22. Y. Feng, X. Ji, J. Duan, J. Zhu, J. Jiang, H. Ding, G. Meng, R. Ding, J. Liu, A. Hu and X.

Huang, J. Solid State Chem. 190 (2012) 303-308.

23.　M. Law, L. E. Greene, A. Radenovic, T. Kuykendall, J. Liphardt and P. Yang, J. Phys. Chem. B 110 (2006) 22652-22663.

24.　C. Gao, X. Li, B. Lu, L. Chen, Y. Wang, F. Teng, J. Wang, Z. Zhang, X. Pan and E. Xie, Nanoscale 4 (2012) 3475-3481.

25.　P. Tiwana, P. Docampo, M. B. Johnston, H. J. Snaith and L. M. Herz, ACS Nano 5 (2011) 5158-5166.

26.　W.-Q. Wu, H.-L. Feng, H.-S. Rao, Y.-F. Xu, D.-B. Kuang and C.-Y. Su, Nat. Commun. 5 (2014) 3968.

27.　H.-L. Feng, W.-Q. Wu, H.-S. Rao, L.-B. Li, D.-B. and Kuang, C.-Y. Su, J. Mater. Chem. A 3 (2015) 14826-14832.

28.　H.-L. Feng, W.-Q. Wu, H.-S. Rao, Q. Wan, L.-B. Li, D.-B. Kuang and C.-Y. Su, ACS Appl. Mater. Interfaces 7 (2015) 5199-5205.

29.　W.-Q. Wu, B.-X. Lei, H.-S. Rao, Y.-F. Xu, Y.-F. Wang, C.-Y. Su and D.-B. Kuang, Sci. Rep. 3 (2013) 1352

30.　W.-Q. Wu, Y.-F. Xu, H.-S. Rao, C.-Y. Su and D.-B. Kuang, J. Am. Chem. Soc. 136 (2014) 6437-6445.

31.　S. H. Ahn, D. J. Kim, W. S. Chi and J. H. Kim, Adv. Mater. 25 (2013) 4893-4897.

32.　D. O. Miles, P. J. Cameron and D. Mattia, J. Mater. Chem. A 3 (2015) 17569-17577.

33.　A. Ramirez-Canon, D. O. Miles, P. J. Cameron and D. Mattia, RSC Adv. 3 (2013) 25323-25330.

34.　S. H. Ahn, W. S. Chi, J. T. Park, J. K. Koh, D. K. Roh and J. H. Kim, Adv. Mater. 24 (2012) 519-+.

35.　C. S. Lee, J. Y. Lim, W. S. Chi and J. H. Kim, Electrochim. Acta 173 (2015) 139-147.

36. W. S. Chi, J. K. Koh, S. H. Ahn, J.-S. Shin, H. Ahn, D. Y. Ryu and J. H. Kim, Electrochem. Commun. 13 (2011) 1349-1352.

37. R. Al-Gaashani, S. Radiman, A. R. Daud, N. Tabet and Y. Al-Douri, Ceram. Int. 39 (2013) 2283-2292.

38. O. Lupan, G. A. Emelchenko, V. V. Ursaki, G. Chai, A. N. Redkin, A. N. Gruzintsev, I. M. Tiginyanu, L. Chow, L. K. Ono, B. Roldan Cuenya, H. Heinrich and E. E. Yakimov, Mater. Res. Bull. 45 (2010) 1026-1032.

39. N. Rossler, K. Kotsis and V. Staemmler, Phys. Chem. Chem. Phys. 8 (2006) 697-706.

40. Y. Cong, J. Zhang, F. Chen and M. Anpo, J. Phys. Chem. C 111 (2007) 6976-6982.

41. M. Kunat, U. Burghaus and C. Woll, Phys. Chem. Chem. Phys. 5 (2003) 4962-4967.

42. C. Liangyuan, L. Zhiyong, B. Shouli, Z. Kewei, L. Dianqing, C. Aifan and C. C. Liu, Sensors and Actuators, B: Chemical 143 (2010) 620-628.

43. K. Ogata, T. Komuro, K. Hama, K. Koike, S. Sasa, M. Inoue and M. Yano, Phys. Status Solidi 241 (2004) 616-619.

44. F. Kayaci, S. Vempati, C. Ozgit-Akgun, I. Donmez, N. Biyikli and T. Uyar, Nanoscale 6 (2014) 5735-5745.

45. S. H. Ahn, H. Jeon, K. J. Son, H. Ahn, W.-G. Koh, D. Y. Ryu and J. H. Kim, J. Mater. Chem. 21 (2011) 1772-1779.

46. S. H. Ahn, J. H. Koh, J. A. Seo and J. H. Kim, Chem. Commun. 46 (2010) 1935-1937.

47. Y. Wang, E. Chen, H. Lai, B. Lu, Z. Hu, X. Qin, W. Shi and G. Du, Ceram. Int. 39 (2013) 5407-5413.

48. A. K. Chandiran, M. Abdi-Jalebi, M. K. Nazeeruddin and M. Grätzel, ACS Nano 8 (2014) 2261-2268.

49. Q. F. Zhang, C. S. Dandeneau, X. Y. Zhou and G. Z. Cao, Adv. Mater. 21 (2009) 4087-4108.

50.   D. C. Look, D. C. Reynolds, J. R. Sizelove, R. L. Jones, C. W. Litton, G. Cantwell and W. C. Harsch, Solid State Commun. 105 (1998) 399-401.

51.   T. Oekermann, D. Zhang, T. Yoshida and H. Minoura, J. Phys. Chem. B 108 (2004) 2227-2235.

52.   F. Fabregat-Santiago, J. Bisquert, E. Palomares, L. Otero, D. Kuang, S. M. Zakeeruddin and M. Gratzel, J. Phys. Chem. C 111 (2007) 6550-6560.

53.   D. J. Kim, S. H. Ahn, C. S. Lee and J. H. Kim, J. Mater. Chem. A 3 (2015) 17644-17651.

54.   S. H. Ahn, D. J. Kim, W. S. Chi and J. H. Kim, J. Mater. Chem. A 3 (2015) 10439-10447.

55.   F. Lodermeyer, R. D. Costa, R. Casillas, F. T. U. Kohler, P. Wasserscheid, M. Prato and D. M. Guldi, Energy Environ. Sci. 8 (2015) 241-246.

56.   H. Wang, J. Li, F. Gong, G. Zhou and Z.-S. Wang, J. Am. Chem. Soc. 135 (2013) 12627-12633.

57.   C. Xu, J. Wu, U. V. Desai and D. Gao, Nano Lett. 12 (2012) 2420-2424.

58.   H. Wang, X. Zhang, F. Gong, G. Zhou and Z.-S. Wang, Adv. Mater. 24 (2012) 121-124.

59.   W. Zhang, J. Li, S. Jiang and Z.-S. Wang, Chem. Commun. 50 (2014) 1685-1687.

Scheme and Figure captions

Figure 1. SEM and TEM micrographs of (a), (d) ZNW, (b), (e) ZNW@TNS (centrifugation) and (c), (f) ZNW@TNS (natural precipitation).

Figure 2. XPS of ZNW and ZNW@TNS nanoparticles; corresponding region of (a) zinc (Zn), (b) titanium (Ti), (c) oxygen (O), and (d) nitrogen (N). (Dashed red lines: Gaussian fitting curve)

**Figure 3.** Surface SEM micrographs of OM (a), (b) w/ H_2O and (c), (d) w/ HCl.

Figure 4. Surface SEM micrographs of (a), (b) ZNW1, (c), (d) ZNW2, and (e), (f) ZNW3 photoanodes with different magnification.

Figure 5. Surface SEM micrographs of (a), (b) ZNW@TNS1, (c), (d) ZNW@TNS2, and (e), (f) ZNW@TNS3 photoanodes with different magnification.

Figure 6. (a) UV-visible light reflectance spectra and (b) photograph of OM, ZNW, and ZNW@TNS photoanodes.

Figure 7. (a) J-V curve and (b) IPCE spectra of qssDSSCs with OM, ZNW, and ZNW@TNS photoanodes, (c) J-V curve of ssDSSC with ZNW@TNS1 photoanode and PEBII solid electrolyte.
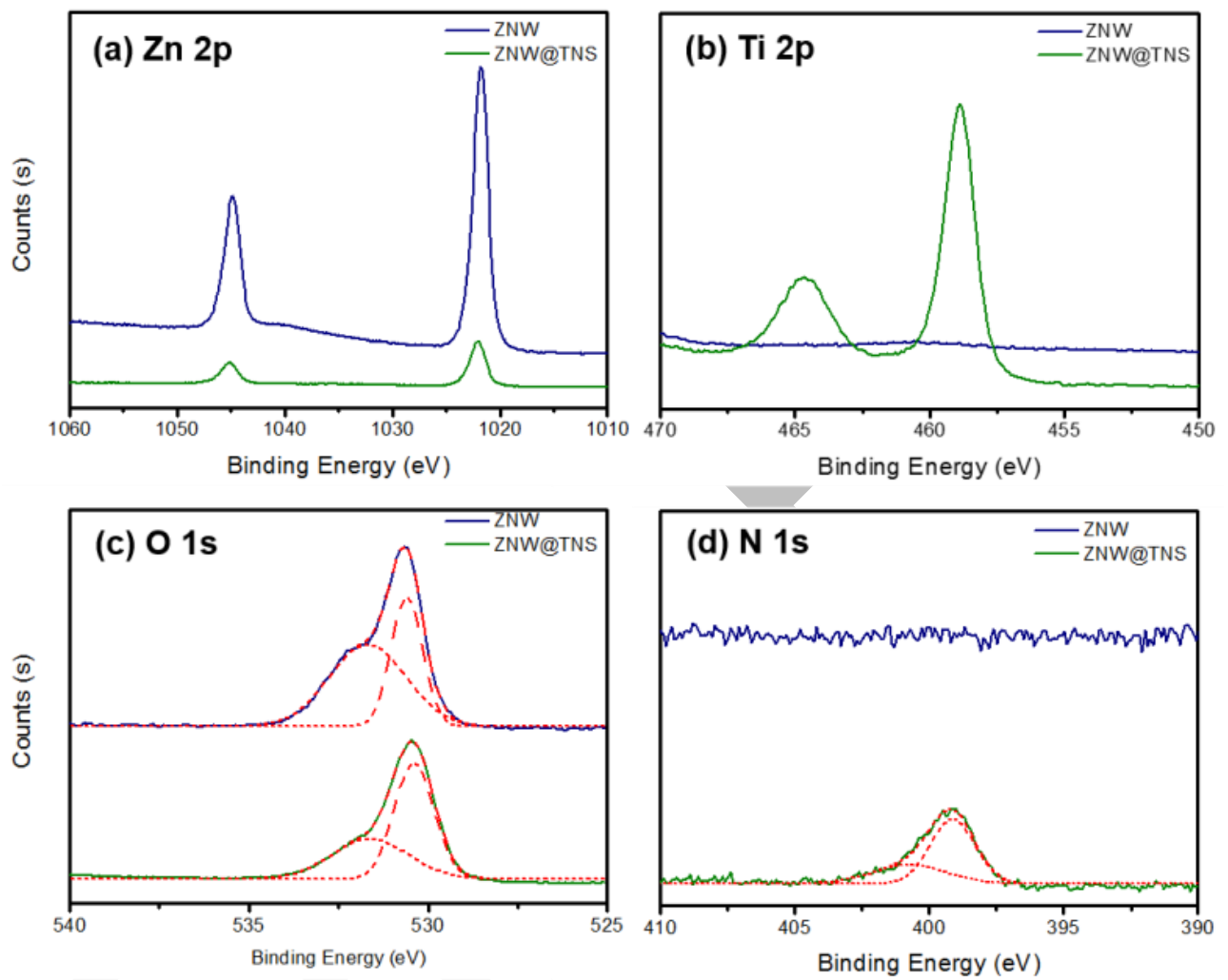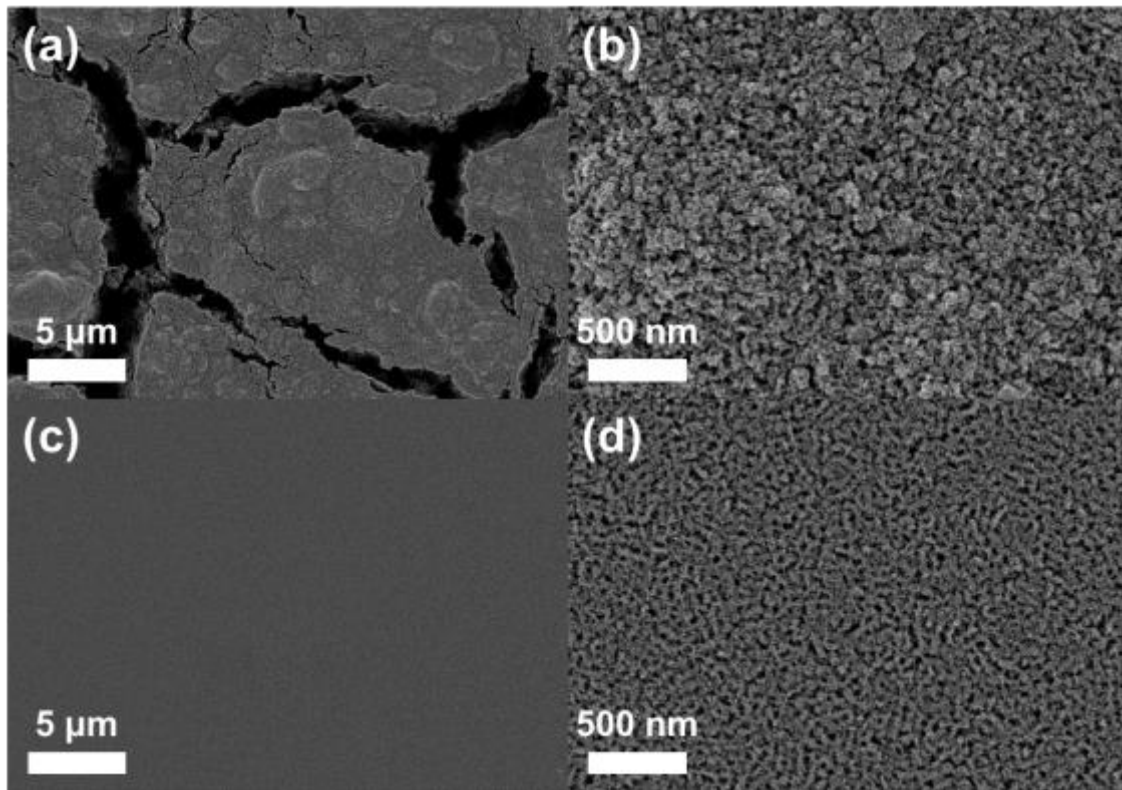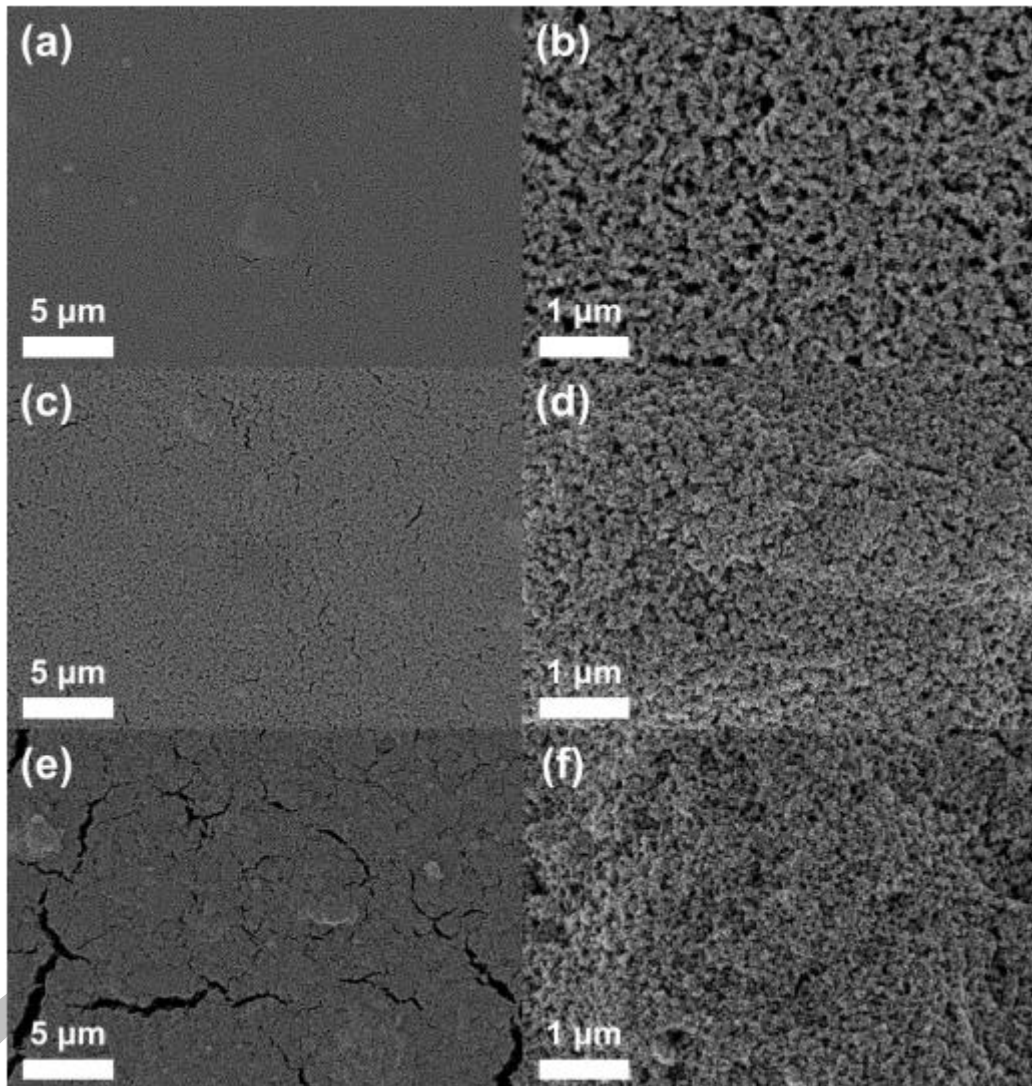
Figure 1
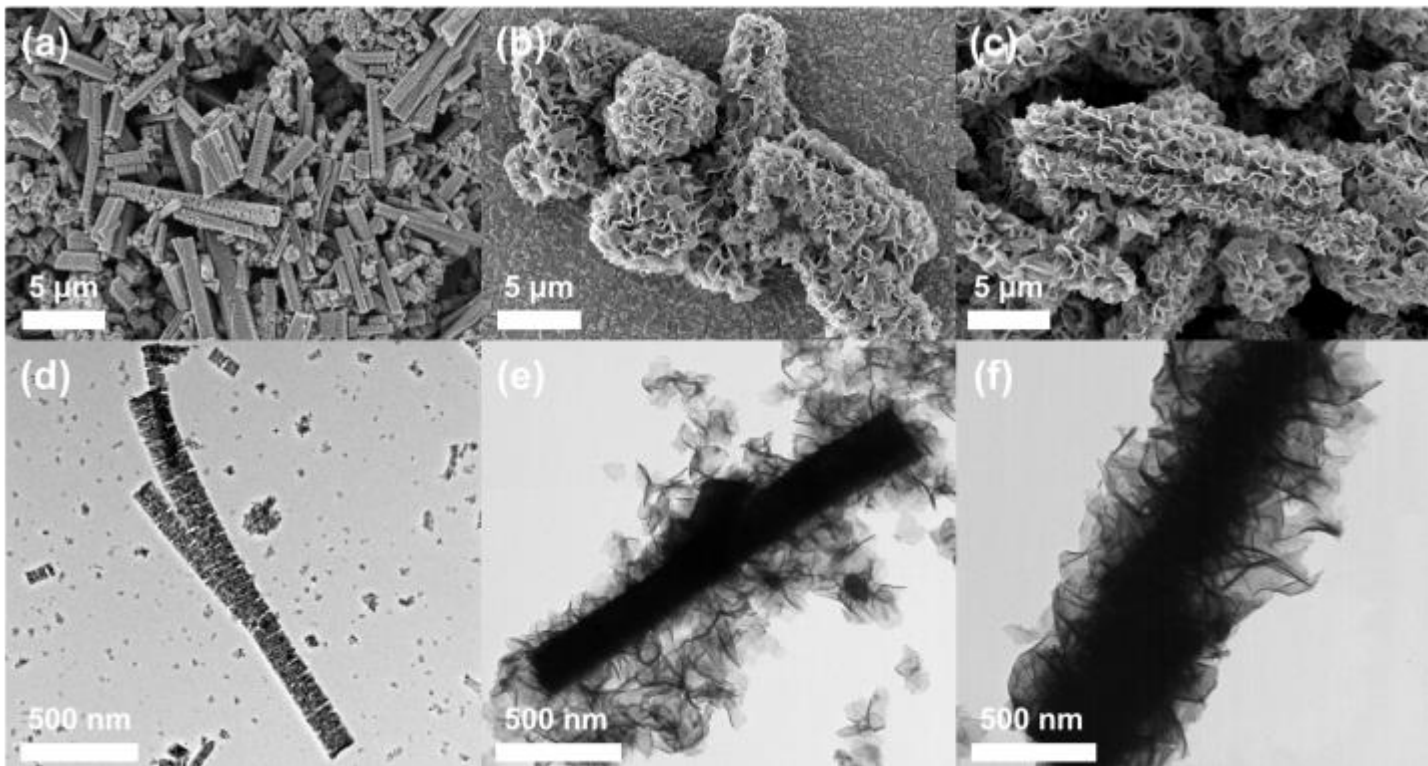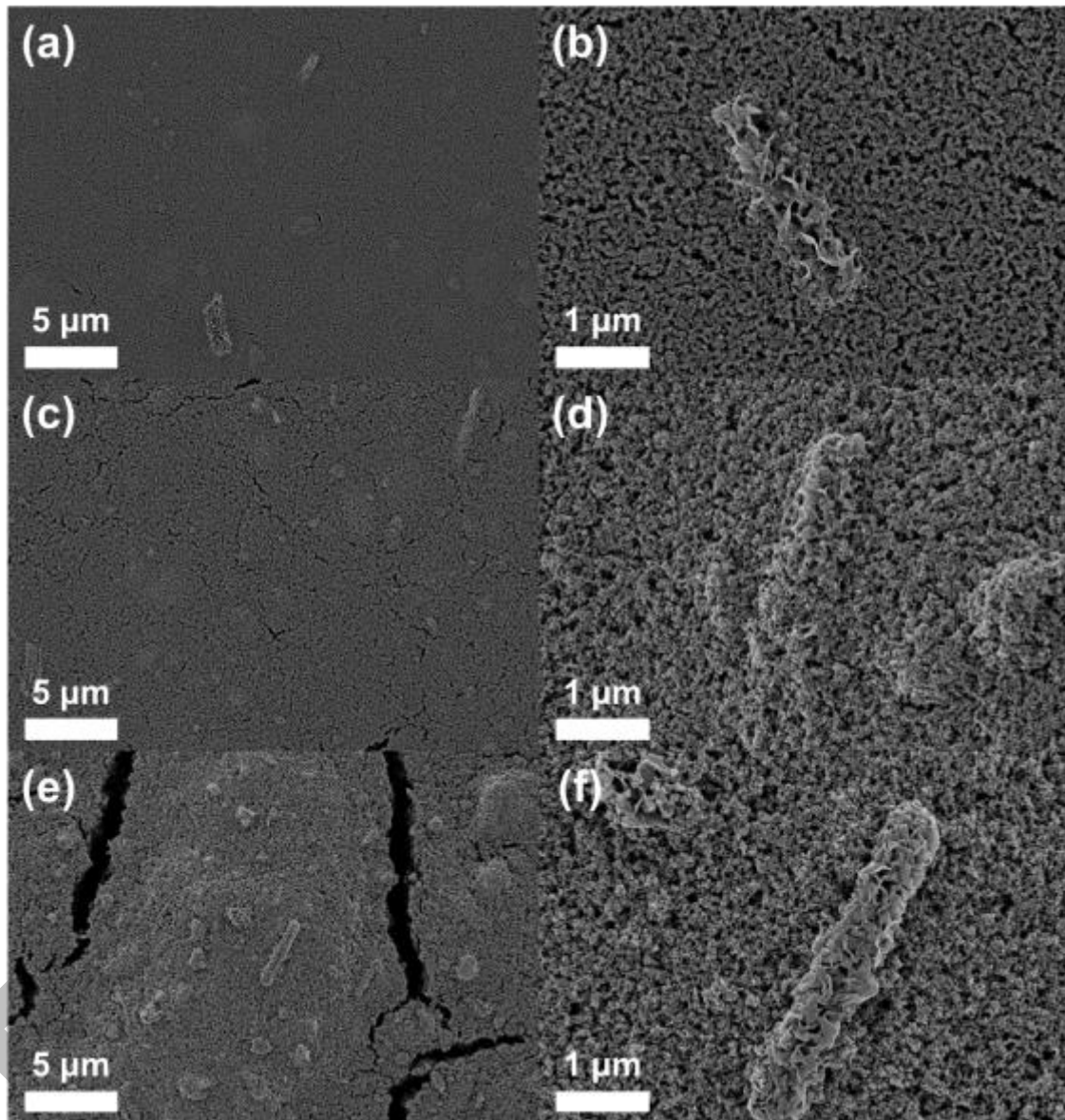
Figure 2

Figure 3
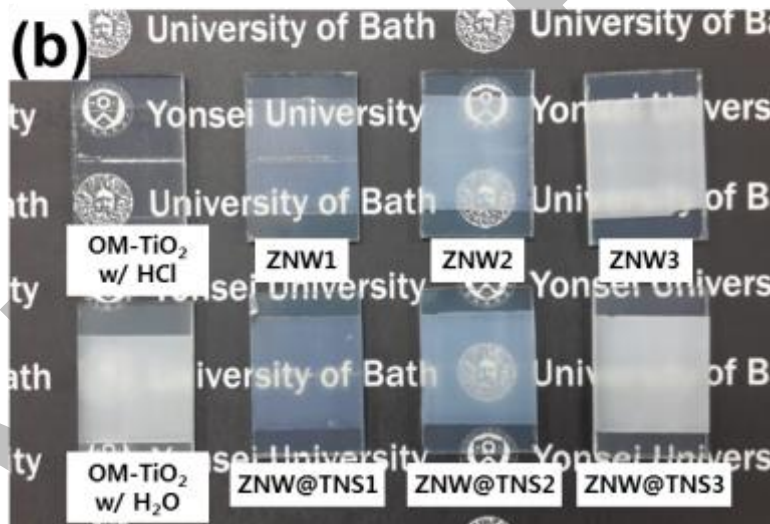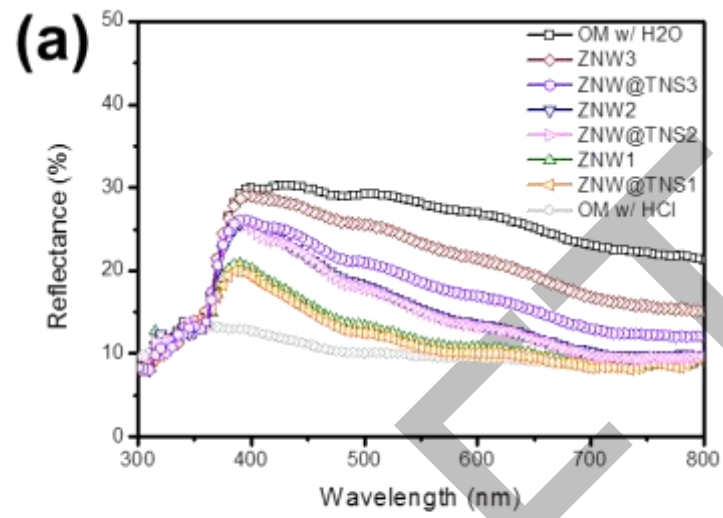
Figure 4

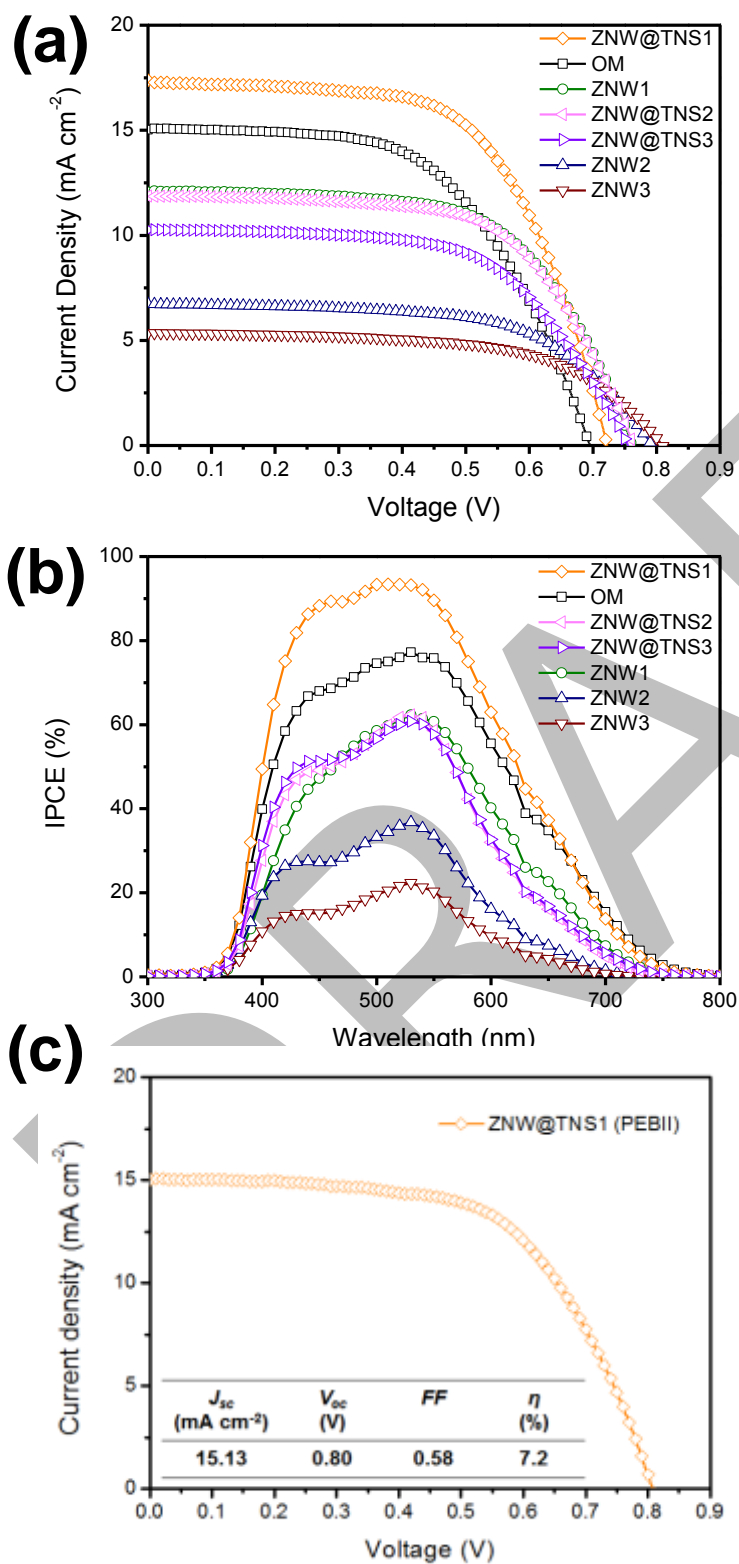**Figure 5**

Figure 6

Figure 7

Table 1. Dye loading, specific surface area and qss-DSSC cell performance for different photoanodes (Thickness = 7 μm)

Photoanode	Dye Loading (nmol cm^{-2})	Specific Surface Area (m^2 g^{-1})	J_{sc} (mA cm^{-2})	Calculated J_{sc} (mA cm^{-2})	V_{oc} (V)	FF	η (%)
OM	110.2	118	15.34	14.70	0.69	0.55	5.78
ZNW1	94.6	105	12.14	10.34	0.76	0.60	5.54
ZNW2	75.7	99	6.70	5.54	0.79	0.60	3.15
ZNW3	39.3	94	5.31	3.23	0.80	0.60	2.57
ZNW@TNS1	125.5	119	17.36	17.50	0.72	0.60	7.46
ZNW@TNS2	90.4	105	11.92	9.92	0.75	0.60	5.42
ZNW@TNS3	73.5	97	10.36	10.14	0.75	0.58	4.49